Pulse line ion accelerator concept

Richard J. Briggs
Science Applications International Corporation, Alamo, California, 94507, USA
(Received 3 April 2006; published 21 June 2006)

The pulse line ion accelerator concept was motivated by the desire for an inexpensive way to accelerate intense short pulse heavy ion beams to regimes of interest for studies of high energy density physics and warm dense matter. A pulse power driver applied at one end of a helical pulse line creates a traveling wave pulse that accelerates and axially confines the heavy ion beam pulse. Acceleration scenarios with constant parameter helical lines are described which result in output energies of a single stage much larger than the several hundred kilovolt peak voltages on the line, with a goal of 3–5 MeV/meter acceleration gradients. The concept might be described crudely as an ''air core'' induction linac where the pulse-forming network is integrated into the beam line so the accelerating voltage pulse can move along with the ions to get voltage multiplication.

DOI: 10.1103/PhysRevSTAB.9.060401 PACS numbers: 29.17.+w

I. INTRODUCTION

In the ''pulse line ion accelerator'' (PLIA) concept described in this paper, a ramped high voltage pulse is applied at the input end of a helical pulse line structure. The resulting traveling wave pulse on the line can accelerate an ion bunch to energies much greater than the peak voltage applied to the line. It should also be possible to achieve an axial acceleration gradient of several MeV per meter with realistic helix parameters.

The development of this concept was originally motivated by a proposal to use moderate energy intense ion beams to heat matter to regimes of interest for studies of high energy density physics (HEDP) and warm dense matter (WDM) [1]. In this approach, very short pulses ($\sim$ a nanosecond or less) of ''medium mass'' ions with energies slightly above the Bragg peak are focused to mm scale spot sizes onto thin target ''foils,'' which may in fact be foams with mean densities of order 10% solid density or less. The high degree of uniformity and efficiency with volumetric and shockless heating of the target to temperatures of order 1 to 10 eV are attractive features in this approach.

The concept presented in this paper is an excellent fit to the accelerator requirements for this HEDP/WDM application. A helical pulse line inserted into a large bore 5–10 T superconducting solenoid can transport and accelerate a singly charged Ne or Na ion bunch with a total charge of order 0.1 to 1 μC, an axial bunch length of 10's of cm, and a radius of a few cm. The required axial compression to bunch lengths of order 1 cm in a neutralized drift compression region following the accelerator is then only a factor of 10–30, which greatly eases the requirements on longitudinal emittance, velocity tilt, and drift distance.

The major attraction of the concept is the very low development and capital cost it promises. The helical pulse line structures are simple to construct and relatively inexpensive. Many features of the wave launching, propagation, dispersion, etc. have already been tested on very inexpensive full scale low voltage models [2]. The pulse power drivers are inexpensive (especially at the very low repetition rates needed for an HEDP user facility) and only a few are needed to accelerate Ne + 1 or Na + 1 (for example) to the required 20–25 MeV energies. Finally, the commercialization of high field superconducting solenoids that has been driven by markets in the billion dollar class, like NMR and MRI, makes them relatively inexpensive compared to the more specialized magnets generally used in particle accelerators. A relatively high acceleration gradient is still essential of course for the overall facility cost to be low, and this remains to be demonstrated.

Presentation of the basic pulse line accelerator concept is the main purpose of this paper. Simple models are developed to provide the design tools needed for a zero-order design of a PLIA system. Subsequent publications are planned that will cover more details on the modeling, experimental results, and computer simulations. Numerical examples will generally use parameters appropriate to the HEDP/WDM application, but otherwise the presentation of the concept should be general enough for readers to judge the suitability of the concept to applications of interest to them.

The outline of the paper is as follows. The basic helical pulse line concept is described in Sec. II. In Sec. III, concepts for coupling the high voltage traveling wave onto the pulse line are described. Simple kinematics analyses of several ion acceleration scenarios are presented in Sec. IV. The maximum energy gain of an ion pulse in an untapered pulse line section is derived, and tapered parameter pulse lines that maintain synchronism between the ions and the traveling wave are analyzed. A ''snowplow'' mode of operation that might be useful in the first acceleration stage is also described, where the wave speed is much faster than the initial ion velocity. In Sec. V a more complete treatment of the electromagnetic fields and wave dispersion at short wavelengths is presented. A simple

 © 2006 The American Physical Society

analysis of beam loading and bunching instabilities is covered in Sec. VI. Conclusions are presented in Sec. VII, including a discussion of phenomena that will place constraints on the design space of a helical pulse line accelerator and on the acceleration gradients that might be achieved.

II. BASIC CONCEPT

A sketch of a helical pulse line of radius "a" located inside of a conducting cylinder of radius "b" is shown in Fig. 1. A dielectric media of permittivity ε is located in the region outside the helix, while the region inside the helix (where the ion beam is transported) is vacuum. To provide continuous radial focusing of an intense ion bunch, the entire cylindrical structure can be inserted into a large bore solenoid magnet.

Physical realizations will typically have a thin insulating cylinder inside the helix to provide the vacuum barrier, and this insulator must sustain the desired pulsed axial voltage gradients of several MeV per meter along its vacuum interface without flashover. The helix might be wound on this insulator, or on an insulating cylinder of slightly larger radius. As we will see, the dielectric media outside the helix will be stressed by pulsed voltages of (typically) several hundred kilovolts; it could be a solid material or an insulating liquid like oil.

The wave speed regime we are considering for ion acceleration is the order of 1%–10% of the speed of light in vacuum, and the axial wavelength spectrum of interest is large compared to the helix radius. In this regime, the helical line can be modeled as a transmission line with equivalent inductance and capacitance per unit length of

$$L_0 = \pi n^2 a^2 \mu_0 (1 - a^2/b^2) \tag{2.1}$$

$$C_0 = \frac{2\pi\varepsilon}{\ln(b/a)}, \tag{2.2}$$

respectively, where n is the number of turns per meter of the helix and the "shielding factor" $(1 - a^2/b^2)$ in the inductance accounts for the fact that the net axial flux of the microsecond time scale pulsed axial magnetic fields within the conducting cylinder must vanish.

Defining the voltage from the helix to the outer cylinder as $V(z, t)$, and the $+z$ directed current in the helix as $I(z, t)$ (see Fig. 1), the transmission line equations in the long axial wavelength regime are

$$\frac{\partial V}{\partial z} = -L_0 \frac{\partial I}{\partial t} \tag{2.3}$$

$$\frac{\partial I}{\partial z} = -C_0 \frac{\partial V}{\partial t}. \tag{2.4}$$

The well-known solutions to these elementary transmission line equations are traveling waves of arbitrary shape, i.e., for the wave traveling in the $+z$ direction

$$V(z, t) = V_+(z - v_c t) \tag{2.5}$$

with $v_c = (L_0 C_0)^{-1/2}$, the circuit wave speed. The current $I(z, t)$ is equal to $V(z, t)$ divided by the characteristic impedance of the transmission line $Z_0 = (L_0/C_0)^{1/2}$. With the output end of the helical pulse line terminated in this characteristic impedance, the $+z$ traveling wave in Eq. (2.5) is the total solution for all time.

The axial electric field inside the helix is approximately constant in radius in this long wavelength approximation, so the ions are all accelerated by a circuit field given by

$$E_z = -\frac{\partial V}{\partial z}. \tag{2.6}$$

A typical example of the voltage pulse we consider is shown in Fig. 2. At the input end of the helix a pulse power source (using one of the coupling schemes discussed in Sec. III) creates a ramped voltage waveform *in time* at a fixed z position (say $z = 0$) of the form shown in Fig. 2. In the (approximately) linear ramp region, the voltage goes from $-V_o$ to $+V_o$ in a time scale of order τ_c, where as a precise definition of τ_c we might use

$$\tau_c = \frac{2V_0}{(\partial V_+/\partial t)_{\text{at the center of the ramp}}}. \tag{2.7}$$

At some later time $t = t_1 > \tau_c$, a "snapshot" of the voltage on the line vs z is as shown in Fig. 3. This voltage

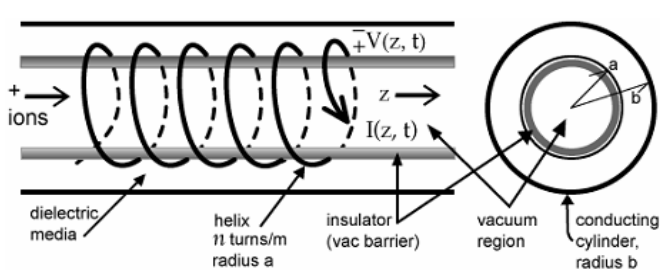

FIG. 1. Helical pulse line.

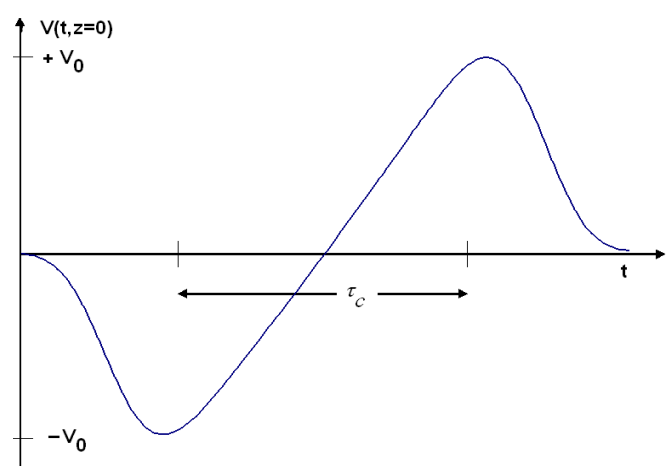

FIG. 2. (Color) Voltage waveform at the helix input ($z = 0$).

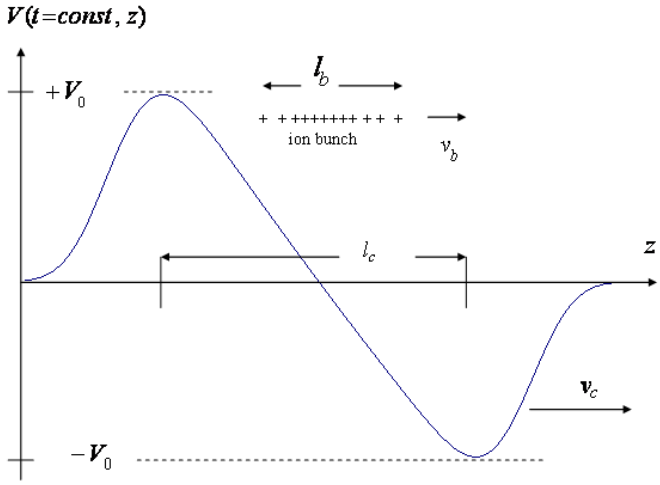

FIG. 3. (Color) Snapshot of voltage on helix vs z.

waveform propagates down the line with the circuit speed v_c maintaining a constant shape (in the long wavelength limit). The negative ramp extends over a distance of order $l_c = v_c \tau_c$ controlled by the applied pulse power waveform. An ion bunch located in the ramp region moving with a velocity v_b will be accelerated by the axial electric field given by Eq. (2.6). This axial circuit electric field vs z is shown in Fig. 4, at the time $t = t_1$. In the sketch shown, this field is approximately constant over the ramp region, with an average value of

$$E_{\rm acc} = \frac{2V_0}{l_c} \tag{2.8}$$

accelerating the ion bunch located in the ramp region.

Note that a bipolar voltage pulse like that shown in Fig. 2 would generally be preferred because it maximizes the axial acceleration gradient for a given limit on the radial electric field gradient outside the helical line. In Fig. 4, a slight negative ramp on the electric field is indicated, including the option of a "bump" on the tail of the ramp. Features like these are available in this concept, using

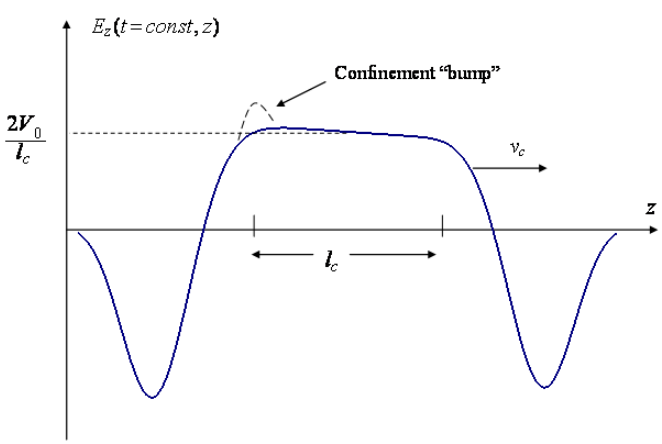

FIG. 4. (Color) Snapshot of accelerating electric field vs z.

appropriate fine-tuning of the pulse power source waveform, to provide axial focusing and/or axial confinement of the ion bunch. (These features are similar to the "ear fields" in the induction linac approach to heavy ion fusion.) Note also that, in the final accelerator section, a much more vigorous negative ramp in the electric field waveform can be used to impart an inward compression to the beam for neutralized drift compression in ion-driven HEDP applications.

The basic acceleration process involving ions "surfing" on a traveling wave is of course superficially very similar to the acceleration of an ion bunch in a radio-frequency linear accelerator (RF linac). Some important differences are the fact that the axial confinement gradients and the acceleration gradients are independent "knobs" in the pulse line ion accelerator, controlled by "tweaking" the voltage waveform of the pulse power driver (rather than the phase of the bunch in the RF bucket). In addition, in many cases of interest (as we discuss in Sec. IV), the ion speed is far from synchronism with a *constant velocity* circuit traveling wave. In these cases the ion bunch "rides up and down" the accelerating ramp shown in Fig. 3 in the acceleration process; the whole length of this acceleration stage is about one synchrotron period in RF accelerator terms.

Indeed, the PLIA in many ways is more closely related to induction accelerator technology than RF accelerator technology, especially in the use of pulse power technology as the driver. The concept might be described crudely as an "air core" induction linac with a pulse-forming network integrated into the beam line creating an accelerating voltage pulse that moves along with the ions. This traveling wave feature and the voltage multiplication it produces are key advantages over the more standard "standing wave" induction linac architectures.

The oil dielectric helix constructed at LBNL [2] provides a useful concrete example of the concept. The first version of this 1 m long helix was designed for a low frequency wave speed of 2.9×10^6 m/s, appropriate for initial potassium ion energies around 200–400 keV with pulse voltages on the helix of ± 200 keV or more. The helix radius is 8.1 cm, the ground return radius 11.75 cm, and the helix pitch 159 turns/m. With a dielectric permittivity (oil) of 2.3, the low frequency capacitance is 344 pF/m, the inductance is 346 μH/m, and the characteristic impedance is about 1 kilo-ohm.

III. INPUT COUPLERS

"Direct coupling" of the pulse power source output onto the helix, as sketched in Fig. 5, is perhaps the most straightforward approach to consider first. At the input end of the helix, where peak voltages of $\pm V_0$ are applied, control of the gradient along the vacuum insulator in the region in front of the helix is required. The resistive column indicated in Fig. 5 serves this purpose. Note that, as the ion bunch passes through this resistive column

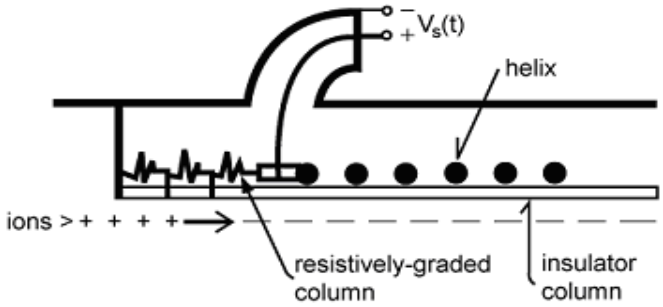

FIG. 5. Direct coupling.

region, a head to tail energy variation will be induced along the ion bunch by the time varying voltage applied to the helix (assuming the timing is set so the whole ion bunch is injected into the ramp region of the traveling wave as in Fig. 3). This is one of the complications with this approach, although the resulting energy variation could be compensated in various ways.

In the design of direct coupling systems, the feedthroughs must withstand the full peak voltage of the traveling wave on the helix. The stray capacitance of the feedthroughs and the input coupler region must also be accounted for and controlled. The characteristic impedance of helical transmission lines (which appear as a resistive load on the drive system at the input end) are the order of a kilo-ohm for typical ion accelerator designs, so the voltage rise time, a product of this characteristic impedance times the stray input capacitance, can be appreciable.

The traveling wave on the helix could also be launched using the induction cell coupler shown in Fig. 6. Using the output voltage of the induction cell to drive the helix as shown in Fig. 6 eliminates the need for the resistive column and it also eliminates the head to tail energy variation it induces on the ion pulse. The gap capacitance of the induction cell might impose a significant constraint on the ramp rise time, however, as in the direct coupling case.

A third method for driving the helix is the transformer coupler illustrated in Fig. 7. In this approach, the input end of the helix is shorted to the outer cylinder (ground). A primary strap of radius a_p with (typically) only one or two

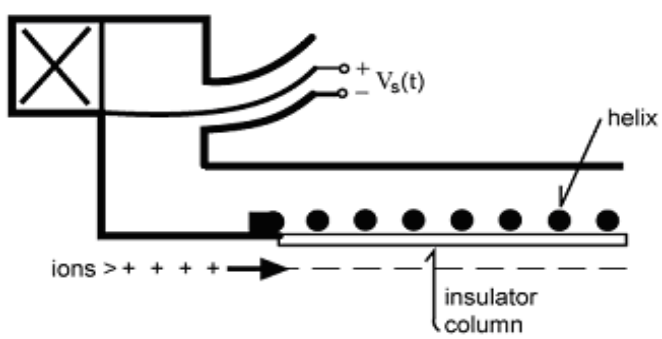

FIG. 6. Induction cell coupler.

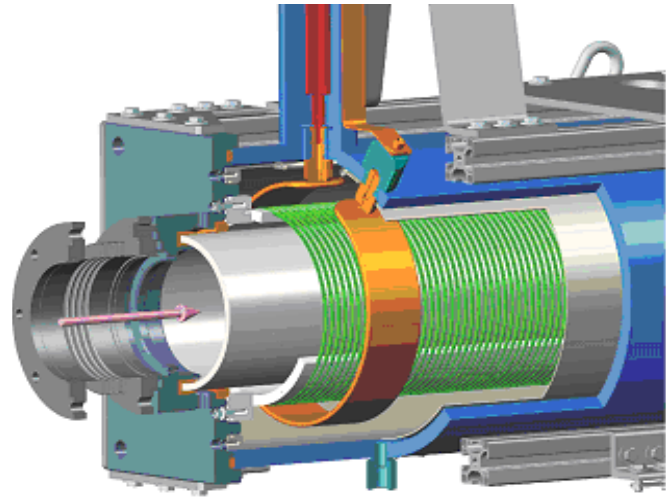

FIG. 7. (Color) One turn transformer drive illustrated on the oil helix [2]. The helix wire (green) is grounded to the outer conducting tube on the left side. (Figure courtesy Matthaeus Leitner, LBNL).

turns is placed near the grounded input end of the helix. A low impedance pulse power source drives current through this primary strap. A fraction of the flux created by the primary strap links the helix, and this flux generates an axial voltage gradient along the input region of the helix.

If the length over which the primary flux linking the helix is "short enough" (according to the criteria derived below), we can think of the input region as a lumped circuit step-up transformer. The voltage on the helix at the end of the flux linkage region, $V_T(t)$, will launch a traveling wave in much the same fashion as if we had connected a direct drive voltage source at that point. A major advantage of the transformer coupler is the large step-up in voltage available. In low voltage tests of models, step-ups of 5:1 or more have been achieved [2]. The corresponding reduction in the feedthrough voltage is a particularly attractive feature of the transformer coupler approach.

A simple model of the transformer coupler can be formulated as follows. Let $I_p(t)$ be the pulsed current on the primary strap, and $B_{zp}(r, z, t)$ the axial magnetic filed created by this primary strap current. The axial flux from the primary current *that links the helix* is

$$\Phi_p(z, t) = \int_0^a B_{zp}(r, z, t) 2\pi r dr. \tag{3.1}$$

This flux adds to the axial flux created by the current in the helix ($\sim L_0 I$), so the transmission line equations now contain the source term

$$\frac{\partial V}{\partial z} = -L_0 \frac{\partial I}{\partial t} - n \frac{\partial \Phi_p}{\partial t}. \tag{3.2}$$

Note that the helix capacitance per meter will be modified near the primary strap since it is grounded on one end to the outer tube. The model could account for this using a z

dependent $C_0(z)$, but we will neglect this effect in our simple zero-order formulation.

The voltage at the input to the primary strap, $V_p(t)$, comes from a mutual inductance term proportional to $\partial I/\partial t$ and the self-inductance term proportional to $\partial \Phi_p/\partial t$. We will neglect the mutual coupling in our zero-order model since it is generally very weak, although it is easy to include it in the model. The spatial structure of the magnetic field created by the primary current is quasi-static in the frequency regime of interest, so the z dependence of $\partial \Phi_p/\partial t$ can be incorporated in a "shape function" $s(z)$ by the definition

$$\frac{\partial \Phi_p(z,t)}{\partial t} \triangleq -V_p(t)s(z) \tag{3.3}$$

for a one turn primary strap. Note that this shape function could be directly measured by applying a pulsed voltage to the primary and measuring the axial flux inside the helix with a magnetic loop, with the helix open circuited at the end. The general shape we would expect is indicated in the sketch in Fig. 8. The peak value of s should be of order a^2/r_p^2, where r_p is the radius of the primary strap, since the primary voltage is proportional to the total area inside the strap while Φ_p is defined as the flux inside the helix area.

A solution for the voltage and current on the helix launched by a one turn primary strap can be obtained by first calculating the Green's function [i.e., the response to a delta function $s(z)$]. The traveling wave amplitude that is launched downstream from the strap ($z > l_p$), with a general functional dependence $s(z)$, is then

$$V(\tau) = \frac{n}{2}\int [V_p(\tau - z_1/v_c) + V_p(\tau + z_1/v_c)]s(z_1)dz_1, \tag{3.4}$$

where $\tau \triangleq t - z/v_c$. The voltage traveling wave has two terms: a direct "radiation" from the flux element at z_1 ($V_p(\tau + z_1/v_c)$), and the radiation in the $-z$ direction that reflects off of the shorted end of the helix [$V_p(\tau - z_1/v_c)$].

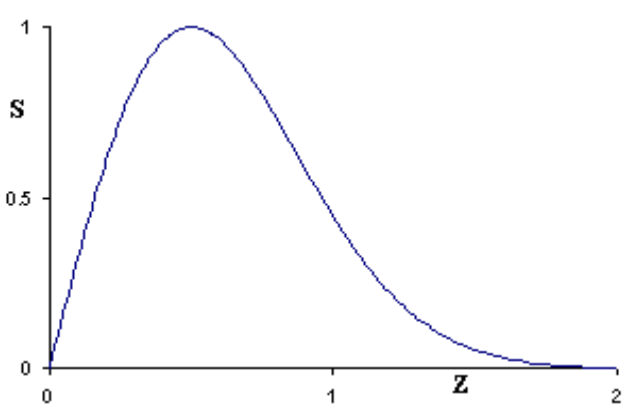

FIG. 8. (Color) Sketch of normalized shape function $S = s(z)/s_0$ vs normalized axial distance $Z = z/l_p$, where $s_0 \sim a^2/r_p^2$ and l_p is a measure of the axial extent of the primary strap.

With a primary voltage waveform of the general form shown in Fig. 2, if the primary voltage ramp length $l_c = v_c\tau_c$ is much longer than the physical extent of the primary flux coupling length (l_p), the solution in Eq. (3.4) reduces to

$$V(\tau) \approx V_p(\tau)n\int s(z)dz \sim nl_p\frac{a^2}{r_p^2}V_p(\tau). \tag{3.5}$$

The voltage step-up is therefore proportional to the turns ratio (nl_p) and also the ratio of the flux linkage areas (a^2/r_p^2) as we would expect.

In an optimum design for high acceleration gradient the helix voltage ramp length l_c would approach the vacuum insulator voltage gradient limit. This vacuum insulator gradient would also set a lower limit on the buildup length of the primary flux linkage (l_p), of course. These two voltage gradients are roughly equal when $l_c/2 \approx l_p$ with the bipolar waveform shown in Fig. 3. In this case, the relation between the primary voltage waveform and the waveform of the helix traveling wave is more complicated.

To illustrate this, we consider the simple sawtooth waveform on the primary voltage shown in Fig. 9 with a ramp duration 2 T equal to $2l_p/v_c$, and a step function dependence of $s(z)$ [$s(z) = s_0$ over $0 \le z \le l_p$ and zero beyond]. The resulting waveform of the transmitted voltage on the helix is also shown in Fig. 9. Note that, in addition to the smoothing of the transmitted wave, the peak amplitude is $\frac{1}{2}$ the value that would be obtained with a much longer ramp length on the voltage waveform applied to the primary [Eq. (3.5)]. The voltage step-up with a transformer coupler

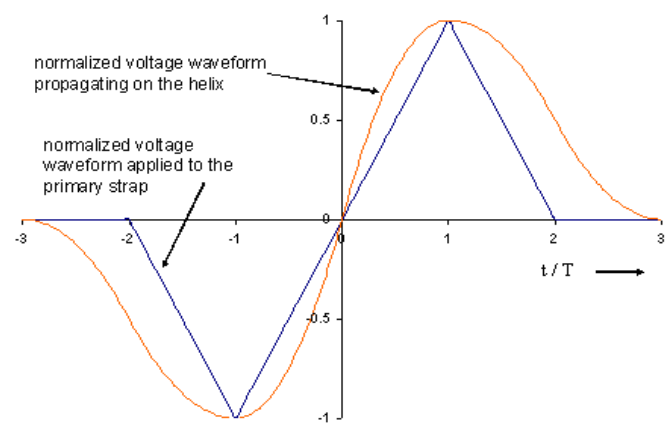

FIG. 9. (Color) Simple example of waveform smoothing when the primary flux coupling length is $\sim\frac{1}{2}$ the helix voltage waveform ramp length. The primary voltage waveform $V_p(t)$ is shown in blue, where the peak amplitude of the voltage is normalized to unity and the time (t) is normalized by $T = l_c/2v_c = l_p/v_c$. The resulting voltage waveform $V(\tau)$ propagating down the helix vs the delayed time $\tau = t - z/v_c$ (also normalized) is shown in red, normalized by its peak amplitude $= ns_0l_p/2$.

depends on the waveform, as this simple example illustrates.

The smoothing illustrated in Fig. 9 is a general property of this transformer coupling configuration. Transforming Eq. (3.4) into the frequency domain, the spectral amplitude of the transmitted voltage is

$$V(\omega) = nS(\omega)V_p(\omega), \tag{3.6}$$

where the transformer coupling function in the frequency domain has the form of a low pass filter

$$S(\omega) = \int s(z)\cos(\omega z/v_c)dz. \tag{3.7}$$

This smoothing is actually a useful property of this coupling method, since as discussed in detail in Sec. V we need to limit the bandwidth of the transmitted voltage to avoid distortion of the waveform as it propagates, and/or radial structure (decay) of the high frequency components of the axial electric field.

Note that the "natural smoothing" of the waveform launched on the helix also helps to limit the axial gradient when "nonideal" primary drive waveforms are used. As a very simple example to illustrate this point, consider a step function voltage drive waveform applied to the primary with the same step function dependence of $s(z)$ [$s(z) = s_0$ over $0 \leq z \leq l_p$ and zero beyond]. The voltage waveform launched on the helix has the form shown in Fig. 10; the maximum axial gradient of the traveling wave on the helix created by this instantaneous step rise is limited to

$$E_z \approx \frac{V_{\max}}{2l_p}. \tag{3.8}$$

A distributed helical transformer is another coupling scheme that might prove useful. The basic idea is to construct a second concentric helix with a radius very close to the outer conducting tube radius ($r = b$), and (possibly) with a higher dielectric constant material between it and the outer cylinder resulting in a much higher capacitance per meter for the outer helix. The turns per meter would be much less than on the main helix (n), but adjusted to make the wave speeds approximately equal. A wave launched on the outer helix, which acts as the "primary", propagating in the $+z$ direction (say) would gradually transfer its energy over to a synchronous $+z$ traveling wave on the main helix. (For a discussion of the behavior of coupled mode systems like this where the coupling is very weak, see, for example, Louisell [3].) Since the outer helical line has a characteristic impedance much less than the main helix, a voltage step-up should be produced. (A simple model calculation indicates that the step-up is approximately equal to the square root of the ratio of the capacitances of the two lines).

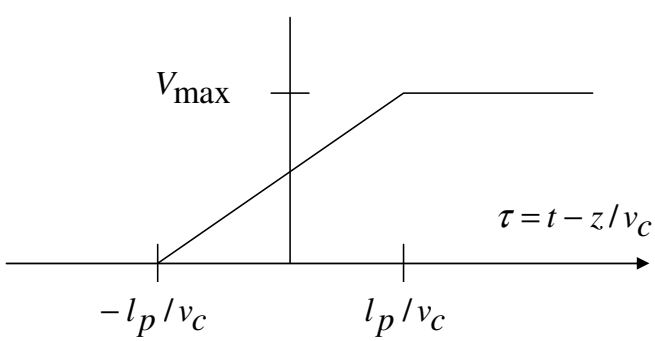

FIG. 10. Voltage waveform launched on a helix by a step function voltage applied to the primary of the transformer.

A detailed analysis of this distributed helical transformer scheme is beyond the scope of the present paper. However, we should point out that the distributed coupling concept might be especially useful as a "directional coupler" in a "repeater station" where we want to regenerate the wave on a helix. Examples of where this might be desirable include heavily beam loaded systems, or where the helix is tapered and the wave amplitude needs to be regenerated as discussed in Sec. IV.

IV. ACCELERATION SCENARIOS

For intense slowly moving ion beams, a large bore superconducting solenoid is a good choice to provide the required continuous radial focusing. In a continuous solenoid, the equilibrium beam radius of a space charge dominated beam is independent of the particle energy, and proportional to the square root of the line charge density. Transporting the ion pulse with a constant axial length is therefore a natural acceleration scenario to use with solenoidal focusing, since it keeps the beam radius at its constant matched value. Constant beam length is also a very good fit to the pulse line accelerator, of course.

As an example applicable to the HEDP objective, the equilibrium beam radius of a Ne + 1 beam with a line charge of 1 μC per meter is $12/B$ cm, with B the solenoid field in Tesla (e.g., 2.4 cm in a 5 T field). A total charge of 0.1 to 0.2 microcoulombs in the bunch can then be obtained with axial bunch lengths of 10 to 20 cm, short enough to fit inside a 20–30 cm ramp length of a traveling wave voltage pulse on the helical line. At these high line charge densities, a significant "tilt" in the axial electric field [e.g., Fig. 4] would also be required ($\sim \pm 0.25$ to 0.5 MeV/m) if continuous axial focusing is desired. (At higher particle energies, the axial focusing might be applied periodically rather than continuously since the axial expansion lengths are longer.)

Particle simulation codes are needed to adequately treat the radial and axial dynamics of intense ion bunches, and these studies are just beginning. To provide initial physical insight into the acceleration dynamics and the various design options, we present here simple kinematics of ion bunches in several acceleration scenarios ignoring the axial space charge forces and the beam loading discussed in Sec. VI (i.e., the limiting case of low intensity bunches).

These analyses can also be useful as the first step in an iterative design process to define the axial focusing requirements with higher bunch intensities.

A. Untapered pulse line

The first case we consider is acceleration in a pulse line with constant L and C parameters. Consider an ion bunch of length l_b initially located at the front end of the traveling wave ramp region, where all the ions move with the initial velocity v_{bi} (see Fig. 3). With a constant slope on the ramp going from $+V_0$ to $-V_0$ over the length l_c, the accelerating field is constant over the ramp region and equal to $2V_0/l_c$, so the ion bunch maintains a constant length as it is accelerated. We define the initial velocity "slippage" as

$$\Delta v = v_c - v_{bi}.$$

Consider first a very short bunch of ions ($l_b/l_c \to 0$). If we go into a reference frame moving with the circuit velocity, the ions are initially moving backwards from the front of the ramp with a velocity Δv. The condition for this short bunch to "ride up and down" the accelerating ramp while still remaining "trapped" by the wave is

$$(\Delta v)^2 \leq 2v_0^2, \tag{4.2}$$

where we define $v_0 \equiv (2qV_0/M)^{1/2}$, the speed of an ion accelerated through a potential V_0. At the position where the short ion bunch arrives back at the front of the ramp region (the maximum energy gain possible with this untapered line), its velocity in the lab frame is

$$v_{bf} = v_{bi} + 2\Delta v. \tag{4.3}$$

This is a general result for all cases where the ions are trapped by the wave. The maximum velocity gain is where we reach the limit in Eq. (4.2), $v_{bf} = v_{bi} + 2\sqrt{2}\, v_0$, corresponding to a kinetic energy increase at the end of the acceleration process equal to

$$\frac{W_f}{V_0} = 8 + 4\sqrt{2W_{bi}/V_0}. \tag{4.4}$$

Even in the early acceleration stages, where the initial kinetic energy of the ions W_{bi} might be comparable to V_0, an energy gain of 15–20 times the peak voltage on the line can be obtained with a short bunch. This all assumes, of course, that the system length and acceleration gradient are large enough to reach this limit.

The situation where the ion bunch occupies a substantial fraction of the ramp length will generally be the case of greater interest. One would like to choose the voltage ramp length as short as possible to maximize the acceleration gradient, of course. To understand the tradeoffs, we assume that the ion bunch length l_b *is fixed* at its minimum value consistent with the limit on line charge density from radial focusing. The circuit ramp length l_c is then considered to be the free parameter we can vary.

Let $z_b(t)$ be the axial coordinate of the ions at the head of the bunch. Then the "slippage distance" of the bunch head behind the front of the ramp is given by

$$\Delta z = v_c t - z_b(t), \tag{4.5}$$

where we take $t = 0$ as the start of the acceleration process. The maximum energy gain for all the ions will clearly be obtained when the constant length ion bunch "rides up and down" the full extent of the linear voltage ramp without having the tail ions "fall over" the peak of the ramp $at + V_0$ (see Fig. 3). This requires

$$\Delta z_{\max} \leq l_c - l_b, \tag{4.6}$$

where $\Delta z_{\max}$ is the maximum slippage distance, reached at the point where the ions reach synchronism with the circuit wave. Solving for the head ion motion in the assumed constant acceleration field, the limit in Eq. (4.6) is reached with an initial velocity slippage determined by

$$\left(\frac{\Delta v}{v_0}\right)^2 = 2(1 - l_b/l_c). \tag{4.7}$$

The ion velocity at the end of the acceleration process, where the bunch head is leaving the ramp region, is again given by Eq. (4.3). By solving for the system length required to reach this Δv, we can relate the maximum ion energy gain at the output to the system length for various initial ion energies.

Examples with initial ion energies equal to $10V_0$ and $100V_0$ are shown in Figs. 11 and 12, respectively. In both figures, the maximum ion energy gain is normalized to V_0 and the system length is normalized to the ion bunch length l_b. For each value of the system length (with a given beam pulse length and peak voltage V_0), the circuit ramp length and circuit wave speed are both optimized to achieve this maximum energy gain (e.g., see the energy doubling point

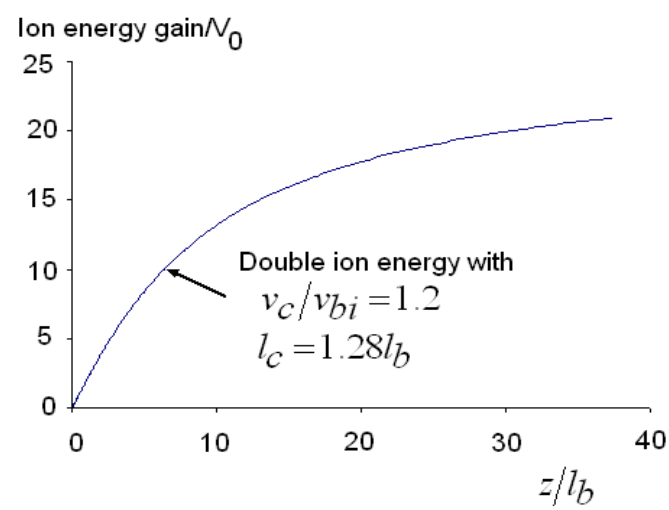

FIG. 11. (Color) Maximum ion energy gain in an untapered line normalized to V_0 vs system length normalized to l_b for $W_{bi} = 10V_0$.

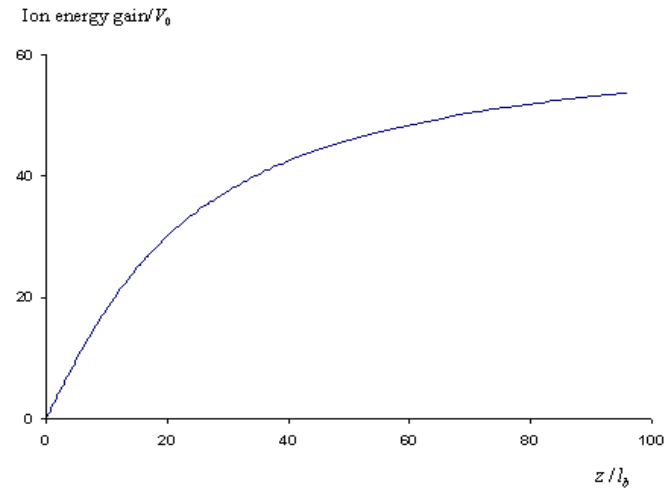

FIG. 12. (Color) Maximum ion energy gain in an untapered line normalized to V_0 vs system length normalized to l_b for $W_{bi} = 100V_0$.

shown in Fig. 11). At very short system lengths, we choose $l_c \approx l_b$ (maximum gradient with a given beam pulse length) and get an energy gain linearly proportional to the system length. As we increase the system length to get a larger gain, we must increase l_c/l_b and the achievable energy gain eventually saturates at the value given by Eq. (4.4).

B. Tapered line with constant impedance

To get larger energy gains from a single pulse line section, it is natural to consider tapering the helical line parameters to maintain synchronism between the circuit speed and the accelerating ions. A variety of tapering schedules might be considered. Here we present one such option, namely, decreasing the inductance and capacitance at the same rate to maintain a constant line impedance as the circuit velocity is increased:

$$L(z) = L_i \frac{v_{ci}}{v_c(z)}, \qquad C(z) = C_i \frac{v_{ci}}{v_c(z)}, \qquad Z_0 = \sqrt{L_i/C_i} = \text{const}, \tag{4.8}$$

with v_{ci} the initial circuit velocity. With this choice, the solution of the transmission line equations are traveling waves of the form

$$V(z,t) = V_0\, f\left(t - \int_0^z \frac{dz'}{v_c(z')}\right), \tag{4.9}$$

$$I(z,t) = V(z,t)/Z_0. \tag{4.10}$$

We choose the usual ramp waveform for $V_0 f(\tau)$ illustrated in Fig. 2 with peak amplitudes of $\pm V_0$. The constant impedance tapering, besides making the "WKB-like" solutions *exact* solutions, has the special property of maintaining a constant peak amplitude of the voltage as the circuit velocity speeds up (an obvious result from the standpoint of power conservation). This tapering schedule would therefore be preferred in a pulse line accelerator design with a high initial acceleration gradient, where the radial voltage would tend to approach its breakdown limit.

The axial electric field does weaken as the circuit velocity is increased, however, since for the ramp in Fig. 2

$$E_z = -\frac{\partial V}{\partial z} = \frac{2V_0}{\tau_c v_c(z)}. \tag{4.11}$$

This decrease comes about because the spatial extent of the ramp region spreads out in z as the pulse propagates down the line.

If we taper the line to maintain synchronism between the circuit speed and the accelerating ions, and use Eq. (4.11) as the axial force on the ions, we can derive the ion energy as a function of z as

$$\frac{W_b(z)}{W_{bi}} = \left(1 + 3\frac{V_0}{W_{bi}}\frac{z}{l_{ci}}\right)^{2/3}. \tag{4.12}$$

In Eq. (4.12), $l_{ci} = v_{ci}\tau_c$ is the initial ramp length, which we will set equal to the ion bunch length l_b for purposes of comparing the tapered and untapered lines (i.e., the bunch initially fills the full ramp region).

The normalized ion energy and accelerating gradient are plotted vs $z/L_{\rm acc}$ in Fig. 13, where $L_{\rm acc} \equiv l_b \frac{W_{bi}}{3V_0}$ is the acceleration scale length. (Note that the total ion energy is plotted in Fig. 13, as opposed to the ion energy *increase* plotted in Figs. 11 and 12.) As illustrated in Fig. 13, the local accelerating gradient has dropped to ~70% of its initial value when we reach the point where the ion energy has doubled, and to ~50% when we get to an ion energy of 4 times the initial value.

Tapered and untapered lines are compared in Fig. 14 for the case of an initial ion energy of $10V_0$. In Fig. 14, the system length (normalized to the beam pulse length) is now

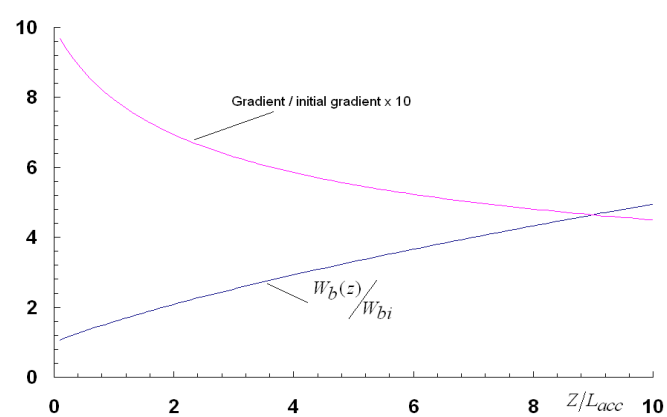

FIG. 13. (Color) Normalized ion energy and normalized gradient vs $z/L_{\rm acc}$ for constant impedance tapered pulse line. (Ion energy/initial ion energy in blue, gradient/initial gradient $\times 10$ in red.)

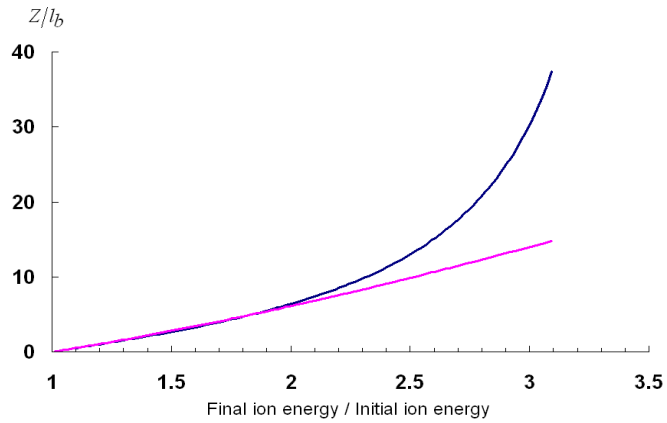

FIG. 14. (Color) Comparison of a tapered (red) and an untapered (blue) helix for $W_{bi}/V_0 = 10$.

the vertical axis while the horizontal axis is the ratio of final ion energy to initial ion energy. We see that, for this initial ion energy, the advantages of tapering the line are not significant until we get well beyond a doubling of the initial ion energy.

The main lesson we draw from this comparison is that the untapered line may be a good choice in many circumstances, depending on the various factors that will ultimately limit the length of a given accelerator stage (dispersion, beam loading, etc.). An untapered helix has more flexibility, of course, since tapering is tied to a particular acceleration schedule. This flexibility and simplicity is particularly attractive for initial experimental studies.

C. Snowplow mode

In the "normal operating mode" of the pulse line ion accelerator discussed in the previous two subsections, the ions are injected during the traveling wave voltage ramp with a velocity reasonably close to synchronism with the circuit speed. The ion bunch length is less than the voltage ramp length, and the ions remain trapped by the pulse line traveling wave throughout the acceleration process. This mode, with or without tapering the line velocity, is the natural choice for the higher energy acceleration stages.

The "snowplow mode" of the helix pulse line described in this subsection could serve as an alternative to the resistive column in a "load and fire injector." It might also be useful in other circumstances. We describe the basic concept here mainly because it illustrates the broad range of possibilities, and flexibility in operating modes, with the pulse line accelerator compared to RF accelerators.

In the load and fire injector proposed to generate ion beams for HEDP, ions from an "accel-decel diode" are loaded into a solenoid transport system to get as high an initial line charge density as possible [4]. In the resistive column version, an axially uniform accelerating electric field is turned on after the ion bunch is loaded, in a time scale short compared to the ion transit time through the system. In addition to the mean energy gain, a velocity tilt is also imparted to the ion bunch because the head of the bunch travels a shorter distance through the resistively graded accelerating column than the tail.

In the traveling wave snowplow mode of a pulse line, a voltage ramp with the shape shown in Fig. 15 is applied at the input of the helical line *after* the ion bunch has been loaded into the helix. This ramp waveform then propagates through the slowly moving ion bunch. In contrast to the "normal operating mode," here the ions slide up the moving voltage pulse and onto the flat top (where the acceleration drops to zero). Choosing a circuit velocity much faster than the initial ion velocity can ensure that this happens. The reason we chose to avoid "trapping" the ions in the present scenario, where the ion bunch is first loaded and then overtaken by the traveling wave, is that orbit overtaking and mixing would result from the trapping. This would likely have a deleterious effect on the longitudinal emittance.

As we show, the moving voltage ramp accelerates the ions and it can also act to compress the bunch length. Note that there is no requirement in the snowplow mode for the bunch length to be less than the voltage ramp length. Note also that, with a long enough flattop on the drive voltage waveform, all the ions will pick up an additional energy of $+V_0$ at the exit where the pulse line is terminated in its characteristic impedance.

As in the previous subsections, the trajectories of the ions with the idealized voltage waveform shown in Fig. 15 are derived ignoring the axial space charge forces. The results are useful for zero-order designs of a snowplow injector, and as analytic checks on more complete computer simulations.

With the voltage waveform in Fig. 15 applied at the input end, the traveling wave propagating on the helix has a constant axial electric field during the ramp portion equal to

$$E_z = V_0/l_c, \tag{4.13}$$

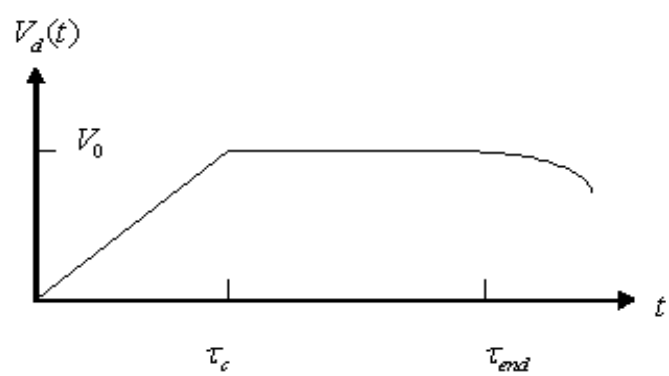

FIG. 15. Drive voltage waveform applied at the input of the helix in the snowplow mode. The ion bunch is loaded prior to $t = 0$.

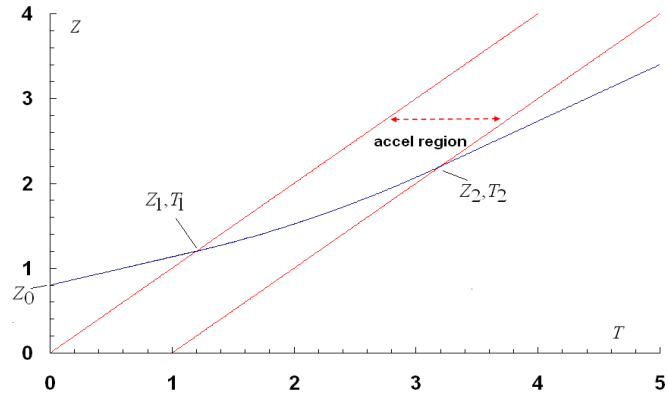

FIG. 16. (Color) Trajectory of a typical ion in the "snowplow mode." The ion is located at the position z_0 when the traveling wave starts to propagate down the helical line.

where, as with the bipolar waveform, the ramp length l_c is the ramp duration τ_c times the circuit propagation velocity v_c. The trajectory of a "typical" ion located initially at $z = z_o$ and moving with an initial velocity v_{bi} is illustrated in Fig. 16. In the figure, the axial coordinate is normalized as $Z = z/l_c$ and time is normalized as $T = t/\tau_c$, so the propagation of the circuit wave has a slope of unity.

The solution for the particle trajectory in Lagrangian coordinates is elementary. Up to the time t_1 when the leading edge of the accelerating field reaches the ion, it moves with a constant initial velocity, so

$$z(z_0, t) = z_0 + v_{bi}t. \tag{4.14}$$

While the ion is in the acceleration region, it has constant acceleration so

$$z(z_0, t) = z_0 + v_{bi}t + \frac{qE_z}{2m}(t - t_1)^2. \tag{4.15}$$

Beyond the point where the ion drops behind the propagating acceleration region (at $t = t_2$), it again moves with a constant velocity v_{bf} that can be calculated from Eq. (4.15).

The algebra remaining is a calculation of the intersection points with the propagating wave (z_1, t_1 and z_2, t_2) in terms of the initial position and velocity of the ion. Readers can fill in these details for themselves; the results are summarized below.

The following are a useful set of normalized parameters:

$$u_0 = \frac{2qV_0}{m(v_c - v_{bi})^2}, \tag{4.16}$$

$$\alpha = 1 - v_{bi}/v_c. \tag{4.17}$$

As with the bipolar waveform, Eq. (4.2), $u_0 = 1$ is the threshold voltage amplitude where an ion with the initial velocity v_{bi} becomes trapped and does not pass through the accelerating wave.

In terms of these parameters, the intersection points are

$$z_1 = v_c t_1 = z_0/\alpha, \tag{4.18}$$

$$t_2 - t_1 = \frac{2\tau_c}{\alpha u_0}(1 - \sqrt{1 - u_0}\,), \tag{4.19}$$

$$z_2 = \frac{z_0}{\alpha} + l_c\left\{\frac{2}{\alpha u_0}(1 - \sqrt{1 - u_0}\,) - 1\right\}. \tag{4.20}$$

The final velocity of the ion after passing through the acceleration region is

$$v_{bf} = v_c(1 - \alpha\sqrt{1 - u_0}\,). \tag{4.21}$$

This velocity is independent of the initial location of the ion, as it should be. All ions drifting with the same initial velocity that pass completely through the acceleration region will therefore exit the helix with the same energy.

The ion bunch will be compressed because the ions located nearest the helix input begin their acceleration before the ions further downstream. To evaluate this bunching in the zero space charge limit, we use the fact that the ions located between z_0 and $z_0 + \Delta z_0$ at $t = 0$ end up located between z and $z + \Delta z$ at a later (fixed) time t. The axial length compression can therefore be calculated from Eq. (4.15) as

$$\frac{\partial z(z_0, t)}{\partial z_0} = 1 - \frac{\alpha u_0}{2\tau_c}(t - t_1), \tag{4.22}$$

where we used the relation $t_1 = z_0/\alpha v_c$. The local line charge density in the vicinity of our "typical ion" therefore increases in time as it is accelerated, as

$$\frac{\lambda_b(t)}{\lambda_{bi}} = \left(\frac{\partial z}{\partial z_0}\right)^{-1}. \tag{4.23}$$

The time scale for this compression is of order $2\tau_c/\alpha u_0$. Using Eq. (4.19) in Eq. (4.22), the final compression of the line charge density (in the absence of any expansion from space charge forces) is

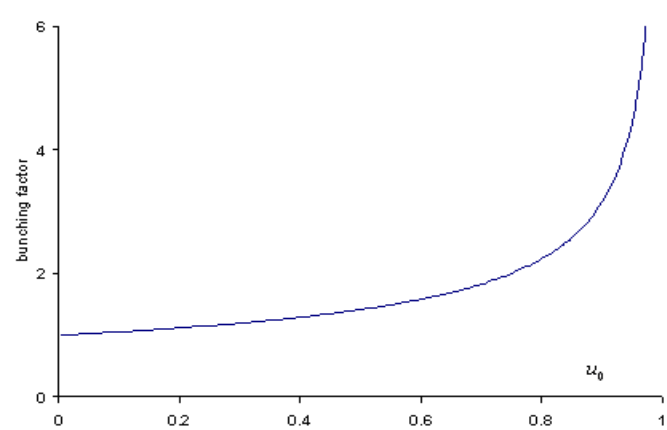

FIG. 17. (Color) Final bunching factor vs $u_0 = V_0/V_{\text{synch}}$.

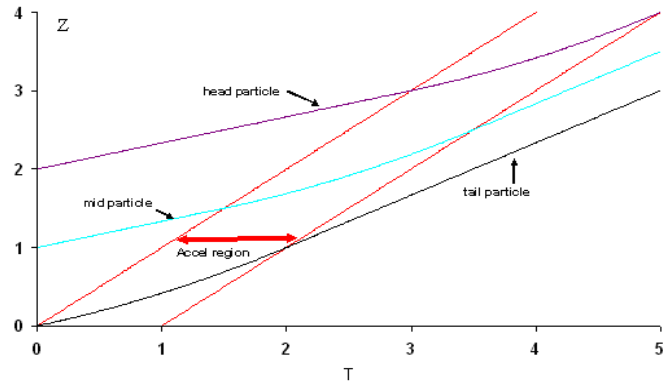

FIG. 18. (Color) Trajectories in an ion bunch that initially extends over two circuit ramp lengths and moves with an initial velocity 1/3 the circuit speed. The bunch is then accelerated in a "snow plow mode" with $u_0 = 3/4$.

$$\frac{\lambda_{bf}}{\lambda_{bi}} = \frac{1}{\sqrt{1 - u_0}}. \tag{4.24}$$

A plot of this bunching factor vs $u_0 \triangleq V_0/V_{\text{sync}}$ is shown in Fig. 17.

An example of the trajectories in an ion bunch with an initial length *twice* the circuit ramp length is shown in Fig. 18. The axial coordinate and time are normalized to the circuit ramp length and duration, respectively, as before. The case presented has the dimensionless parameter $u_0 = 3/4$ (for a bunching factor of 2) and an initial ion velocity 1/3 the circuit velocity ($\alpha = 2/3$), equivalent to an initial kinetic energy of $V_0/3$.

The ion bunch initially extends from $Z = 0$ to $Z = 2$, where the "head particle" is located. If we chose the end of the propagating region of the helix to be at $Z = 4$, the head particle will just finish passing through the accelerating ramp region at the end. (The helical termination resistor is just beyond $Z = 4$.) Note in Fig. 18 that the ion bunch length has been compressed by a factor of 2 at the point the head leaves the helix, as predicted. Note also that at the end of the helix, all the ions exit with the same velocity, namely, 2/3 the circuit velocity, as predicted by Eq. (4.21). This is equivalent to a kinetic energy at the end of the helix of $4V_0/3$, an increase of V_0. As the ions cross the termination resistor region, they *all* pick up an additional kinetic energy of V_0 as long as the pulse applied to the helix has a long enough flat top. Note also that as the ions speed up crossing this termination resistor region, the pulse expands axially by a factor of 1.32, reducing the bunching factor overall to ~1.5.

V. ELECTROMAGNETIC FIELDS AND WAVE DISPERSION

In this section, we present generalized solutions of the electromagnetic fields and the dispersion relation of the helical pulse line. It is actually very straightforward to derive exact solutions to Maxwell's equations using a sheath helix model [5]. Full EM simulations including the actual helical wire geometry have also been carried out [6]. In the regime of interest for heavy ion acceleration, however, where the wave speeds are much less than the speed of light and the transverse dimensions are a small fraction of a free space wavelength, quasistatic approximations to the EM fields should be sufficient. Our major objective here is to develop a self-consistent *quasistatic* sheath helix model, and to show how the transmission line circuit model used in the previous sections is obtained in the long wavelength limit. We will also obtain generalizations of the transmission line model in Fourier space, with k-dependent circuit parameters.

One "tricky" aspect involved in developing these quasistatic field solutions is how to define "voltage" when curl (E) is not zero. It is also important to recognize that the *dominant* source for the electric field is actually the *charge* on the helix wires and not the time derivative of the magnetic flux [7].

The essential approximation involved is a very small pitch on the helix, namely

$$\tan\Psi = \frac{s}{2\pi a} \ll 1, \tag{5.1}$$

where $s = 1/n$ is the wire spacing. A "smooth" approximation to the currents and charges on the helix can then be used to calculate the fields at distances of order $s/2$ or greater away from the wires (essentially a sheath helix model). A current $I(z, t)$ flowing in the helical wires is then equivalent to an azimuthal sheet current

$$K_\theta = \frac{I}{s} \tag{5.2}$$

that is much larger than the axial sheet current $K_z = I/2\pi a$. As a consequence, the dominant magnetic field components are B_Z and B_r created by this azimuthal current; B_θ is smaller by a factor of $s/2\pi a$ ($\sim 1\%$ with typical heavy ion parameters).

An azimuthally symmetric charge per unit length λ (equivalent to a surface charge $\sigma = \lambda/2\pi a$ on the sheath helix) is related to the current in the helical wires by the continuity equation

$$\frac{\partial \lambda}{\partial t} = -\frac{\partial I}{\partial z}. \tag{5.3}$$

This charge acts as a source for an azimuthally symmetric electric field with components E_r, E_z. If we neglect $\partial B_\theta/\partial t$ compared to this charge as the dominant source of the electric field, in a plane with $\theta = \text{const}$ we can use

$$\vec{E} = -\nabla\phi \tag{5.4}$$

to describe the quasistatic electric field. The voltage on the helix is then

$$V(z, t) = \phi(r = a, z, t). \tag{5.5}$$

The final "link" required is the connection between this helix voltage and the time changing axial magnetic flux inside the helix. Using a path integral in Faraday's law that goes *inside* the helix wires at their radius $r = a$ over a distance Δz, encircling the magnetic flux inside the helix $n\Delta z$ times, we have a voltage change over Δz given by

$$\Delta V = -n\Delta z \int_0^a \frac{\partial B_z(r, z, t)}{\partial t} 2\pi r dr. \tag{5.6}$$

In the continuous limit, we have

$$\frac{\partial V(z, t)}{\partial z} = -n \frac{\partial \Phi(z, t)}{\partial t}. \tag{5.7}$$

Here

$$\Phi(z, t) = \int_0^a B_z(r, z, t) 2\pi r dr \tag{5.8}$$

is the total flux inside the helix, created by both the helix azimuthal current and the primary strap current (when transformer coupling is used).

Note that the azimuthal electric field at the helix $E_\theta = -\frac{1}{2\pi a}\partial\Phi/\partial t$ is $s/2\pi a$ smaller than the axial electric field (also order of 1%).

We also emphasize that the "sheath model" of the helix that we are using describes the EM fields accurately outside of radial distances about $s/2$ away from the helix ($\sim$ few mm's typically), since the spatial harmonics needed for a full field solution decay as $\exp - \frac{2\pi m}{s}|r - a|$. The great increase in complexity involved in resolving the EM fields on the fine scale of the wires is unnecessary, except for quantifying the stresses in this region.

A. Computational and analytical field models

The electrostatic and magnetostatic field solutions are governed by solutions to Laplace's equation with

$$\nabla^2\phi = 0, \qquad E = -\nabla\phi, \tag{5.9a}$$

$$\nabla^2\psi = 0, \qquad B = -\nabla\psi. \tag{5.9b}$$

The source for ϕ is the surface charge on the sheath helix $\sigma = \lambda/2\pi a$, which enters in the usual way as a jump condition on the radial derivative of ϕ at $r = a$. Similarly, the source for ψ is the azimuthal sheath helix current $K_\theta = \frac{I}{s}$ that enters as a jump condition on the axial derivative of ψ at $r = a$.

These electrostatic and magnetostatic field solutions are coupled through Eqs. (5.3) and (5.7) [noting the definitions in Eqs. (5.5) and (5.8), which are basically a form of "generalized transmission line equations" connecting $V(z, t)$ and $I(z, t)$. A general computational approach based on this model has been initiated that could incorporate end effects, models of the primary strap, the resistive termination region, ion beam charges as a source for the electric potential, etc. [8]. The essential approximation is the use of a continuous sheet model of the helix, in addition to the quasistatic approximations to Maxwell's equations in the form developed here.

An analytical model of wave propagation on the helix (not including end effects) can also be formulated with this model by going into Fourier space [$\exp(-jkz)$] and solving the Laplace equations subject to the usual boundary conditions. The result can be put in the form of transmission line equations with an equivalent k-dependent capacitance and inductance per unit length. The magnetostatic field $B = -\nabla\psi$ created by $K_\theta = nI$ identifies the inductance per meter $L(k)$ using Eq. (5.8), and the electrostatic potential ϕ created by the line charge λ identifies the capacitance per meter using $\lambda = C(k)\phi(r = a)$.

B. The magnetostatic field and the inductance per meter

The magnetic field inside and outside the helix can be derived from $B = -\nabla\psi$, where $\nabla^2\psi = 0$. The general form of the solution for ψ is

$$\psi = AI_o(kr) \qquad \text{for } r < a,$$

$$\psi = BI_0(kr) + CK_0(kr) \qquad \text{for } r > a. \tag{5.10}$$

We omit the details of the algebra. Using the boundary conditions $B_r(r = b) = 0$, B_r continuous across $r = a$, and $B_z(r = a^-) - B_z(r = a^+) = \mu_0 K_\theta$, the three constants in the solution (5.10) can be determined. For example, the axial field inside the helix is

$$B_z(r) = ka[K_1(ka) - I_1(ka)K_1(kb)/I_1(kb)]\mu_0 K_\theta I_0(kr). \tag{5.11}$$

Using this axial field in Eq. (5.8), the generalized inductance per meter can be identified as

$$L(k) = 2\pi n^2 a^2 \mu_0 \frac{I_1(ka)}{I_1(kb)}[I_1(kb)K_1(ka) - I_1(ka)K_1(kb)]. \tag{5.12}$$

At long wavelengths, an expansion of Eq. (5.12) for $kb \ll 1$ yields the well-known long solenoid result given in

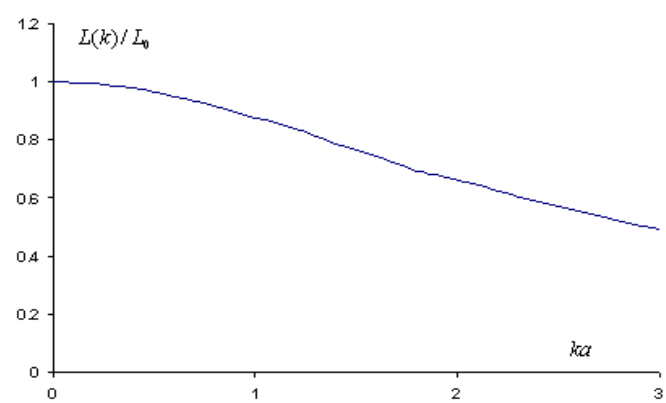

FIG. 19. (Color) Normalized inductance per meter vs ka for $a/b = 0.6$.

Eq. (2.1). The opposite limit, namely $ka \gg 1$, yields

$$L(k) \approx \pi n^2 a^2 \mu_0 / ka. \tag{5.13}$$

The inductance per meter drops off at short wavelengths ($\sim 1/k$) because the mutual coupling of flux from adjacent helix turns decreases. A plot of $L(k)/L_0$ vs ka for the case $a/b = 0.6$ is presented in Fig. 19.

C. The electrostatic field and the capacitance per meter

Setting $\phi = 0$ on the tube wall at $r = b$, the solution of Laplace's equation for the electrostatic potential takes the form

$$\phi = V \frac{I_0(kr)}{I_0(ka)} \qquad \text{for } r < a,$$
$$\phi = D\left(\frac{I_0(kr)}{I_0(kb)} - \frac{K_0(kr)}{K_0(kb)}\right) \qquad \text{for } r > a. \tag{5.14}$$

The constant D is related to V by the continuity of ϕ across $r = a$. For the case where the region outside the helix has a dielectric constant ε while inside $\varepsilon = \varepsilon_0$, the jump condition is $\varepsilon E_r(r = a^+) - \varepsilon_0 E_r(r = a^-) = \lambda/2\pi a$. Relating λ to V identifies the generalized capacitance per meter (after some algebra) as

$$C(k) = 2\pi\varepsilon \frac{I_0(kb)}{I_0(ka)[I_0(kb)K_0(ka) - I_0(ka)K_0(kb)]} - 2\pi(\varepsilon - \varepsilon_0)ka\frac{I_1(ka)}{I_0(ka)}. \tag{5.15}$$

Once again at long wavelengths, an expansion of Eq. (5.15) for $kb \ll 1$ yields the well-known result for the coax capacitance per meter given in Eq. (2.2). The opposite limit of short wavelengths, namely $ka \gg 1$, yields

$$C \approx 2\pi(\varepsilon + \varepsilon_0)ka. \tag{5.16}$$

The capacitance per meter increases at short wavelengths ($\sim k$) because the voltage drop from the helix to the outer wall is reduced by the adjacent surface charges of the opposite sign. A plot of $C(k)/C_0$ vs ka for the case $a/b = 0.6$ and $\varepsilon = \varepsilon_0$ is presented in Fig. 20.

D. Wave speed and impedance

The wave speed (both the phase velocity and the group velocity) approaches a constant value at short wavelengths equal to

$$v_c \approx \frac{\tan\Psi}{\sqrt{\mu_0(\varepsilon + \varepsilon_0)/2}}, \tag{5.17}$$

where $\tan\Psi$ is the helix pitch. When the dielectric constant is the same inside and outside the helix, the waves basically follow the helical pitch of the wires in the short wavelength limit, as might be expected physically. When the dielectric constants are different, the average value governs the speed of the wave at short wavelengths.

As an example, the phase velocity normalized by its long wavelength limit for the case of the same dielectric constant inside and out and $a/b = 0.6$ is presented in Fig. 21.

At long wavelengths, the dielectric constant inside the helix does not enter into the capacitance or the wave speed. Caporaso has noted that the asymptotic value of the wave speed at long wavelengths and short wavelengths can turn out to be the same with appropriate (and reasonable) choices of the dielectric constants and the radius ratio a/b, namely

$$1 + \frac{\varepsilon_0}{\varepsilon} = \frac{(1 - a^2/b^2)}{\ln(b/a)}. \tag{5.18}$$

For example, with a radius ratio $a/b = 0.7$, the Caporaso condition is satisfied with $\varepsilon = 2.3$ outside the helix (e.g., oil) and vacuum inside. One would expect that the dispersion of the wave would be minimized with this choice, but the benefits that accrue from satisfying this criterion will need more quantification before adopting it as an important design constraint.

The wave impedance at short wavelengths drops off $\sim 1/k$ in all cases. The matching of the wave at the termi-

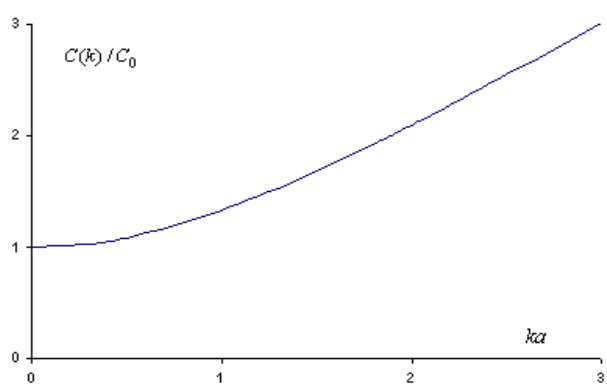

FIG. 20. (Color) Normalized capacitance per meter vs ka for $a/b = 0.6$ and $\varepsilon = \varepsilon_0$.

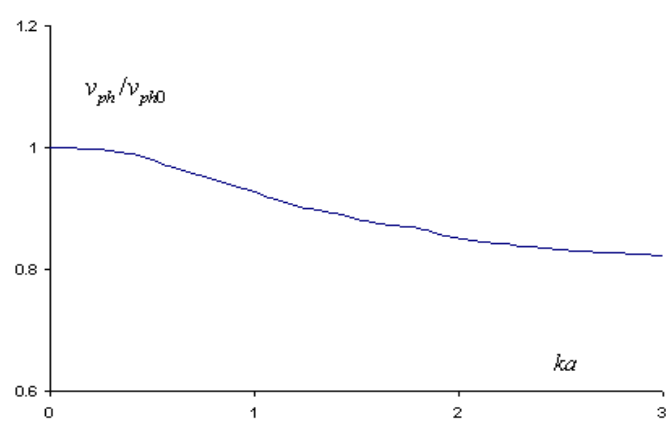

FIG. 21. (Color) Normalized phase velocity vs ka for $a/b = 0.6$ and $\varepsilon = \varepsilon_0$ (note the scale on the vertical axis starts at 0.6).

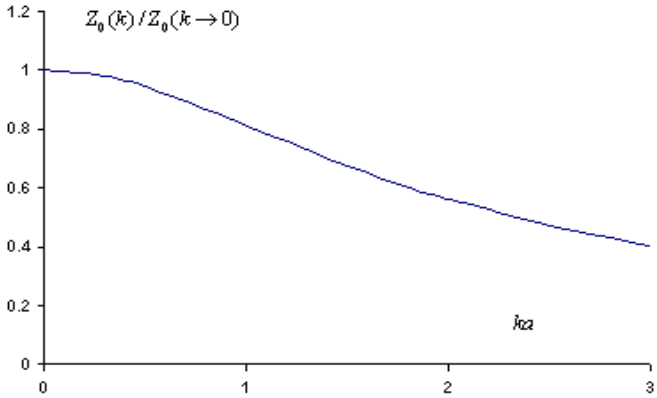

FIG. 22. (Color) Normalized wave impedance vs ka for $a/b = 0.6$ and $\varepsilon = \varepsilon_0$.

nation end will therefore be more difficult to achieve if the pulse has significant energy in the shorter wavelength region ($ka \geq 1$). The impedance normalized by its long wavelength limit for the case of the same dielectric constant inside and out and $a/b = 0.6$ is presented in Fig. 22.

One of the most important reasons to limit the energy in the shorter wavelength region is to avoid the drop off of the axial field on axis when $ka \geq 1$. From Eq. (5.14) we see that the radial dependence of the axial field is $\sim I_0(kr)$, so the field on axis relative to the field at the helix is $\sim 1/I_0(ka)$. A plot of this ratio is presented in Fig. 23.

E. Traveling wave fields

In a forward moving traveling wave (beyond the excitation region) where everything is a function of $t - z/v_c$, we see from Eq. (5.7) that the voltage and magnetic flux have the same $f(t - z/v_c)$ dependence (are "in phase"), with peak values

$$V = nv_c\Phi. \tag{5.19}$$

Therefore, the average axial magnetic field inside the helix (approximately constant in r at long wavelengths) is related to the voltage as

$$\langle B_z\rangle = \frac{V}{\pi a^2 n v_c}. \tag{5.20}$$

For the oil helix parameters discussed in Sec. II, for example, $a \pm 300$ kV voltage pulse produces $a \pm 300$ G pulsed magnetic field.

The axial electric field at the helix, $E_z = -\partial V/\partial z$, is of course "90 degrees out of phase" in space and time with the voltage and axial magnetic field.

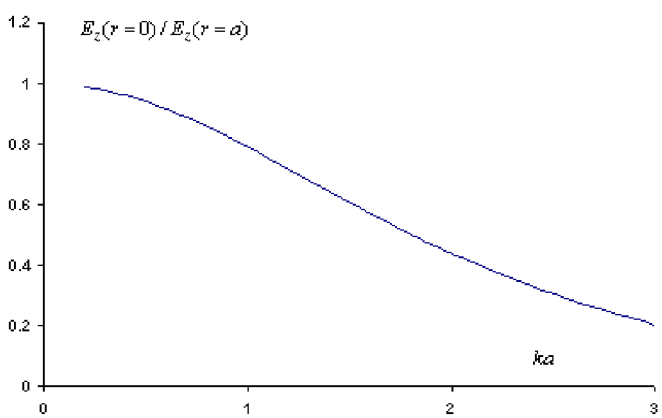

FIG. 23. (Color) Axial electric field on axis divided by the axial electric field at the helix vs ka.

VI. BEAM LOADING

In the previous sections we ignored the ion beam's contribution to the electromagnetic fields propagating on the helix. The fields created by the ion beam are of course an essential part of the energy conversion process, since the electromagnetic power on the helix must diminish as the ions accelerate. The beam-induced fields can also lead to longitudinal bunching instabilities similar to the process that leads to the amplification of microwave power in a traveling wave tube (TWT) helix by an electron beam [3].

Particle simulation codes will be the main tool for a fully self-consistent treatment of beam loading and bunching instabilities at high ion beam intensities. In this introduction to the PLIA concept, we develop elementary models of the beam loading phenomena to gain insight, and to obtain "worst case" estimates of the beam loading and instability gain.

A. Elementary beam loading model

In the long wavelength limit, an ion beam with a line charge density $\lambda_b(z, t)$ induces an opposite image charge on the inside of the helix. The current continuity equation (2.4) then becomes [3]

$$\frac{\partial I}{\partial z} = -C\frac{\partial V}{\partial t} + \frac{\partial \lambda_b}{\partial t}. \tag{6.1}$$

In the nonrelativistic limit, the azimuthal magnetic field created by the ion beam current can be neglected. The derivation of the transmission line equations in Sec. V makes it clear that the second transmission line equation in the long wavelength limit, Eq. (2.3), is not modified by the presence of the ion beam (in the nonrelativistic limit).

As a simple example of ion beam loading consider the voltage and current induced on an untapered helix by an ion beam pulse with a fixed axial profile moving at a constant velocity v_b. The ion beam line charge density is then of the form $\lambda_b(z, t) = \lambda_b(z - v_b t)$. The particular solution of the transmission line equations (6.1) and (2.3) using this ion beam source term in Eq. (6.1) is

$$V_p(z, t) = \frac{\lambda_b(z - v_b t)}{C(1 - v_c^2/v_b^2)} \tag{6.2}$$

and

$$I_p(z,t) = \frac{v_c}{v_b} Y_0 V_p(z,t). \tag{6.3}$$

Note that the "EM radiation" into the helix by the ion beam pulse described by this solution has a singularity when the ion velocity equals the circuit wave speed. If the ion beam pulse enters the helix at $z = 0$ where $V = 0$ (transformer drive, for example), we must also include the homogeneous solution to satisfy the boundary condition, so

$$V(z,t) = \frac{1}{C(1 - v_c^2/v_b^2)}[\lambda_b(t - z/v_b) - \lambda_b(t - z/v_c)], \tag{6.4}$$

for $z > 0$. When the propagating wave reaches the end of the helix, a negative propagating helix wave must be added to Eq. (6.4) to satisfy the appropriate boundary condition at that end.

In most of the acceleration scenarios described in Sec. IV, the ion velocity is not in close synchronism with the circuit velocity. An expansion of Eq. (6.4) for $v_b \to v_c$ should therefore represent an upper bound estimate of the beam loading. This expansion yields a beam-induced voltage increasing linearly with distance,

$$V = z\frac{Z_0}{2}\frac{\partial \lambda_b}{\partial t}. \tag{6.5}$$

With a parabolic bunch shape the beam-induced voltage on the helical line at the synchronous velocity varies linearly across the bunch, so the (decelerating) axial electric field is a constant over the ion bunch. Using $\lambda_b = \lambda_{b0}(1 - 4(z - v_b t)^2/l_b^2)$ in Eq. (6.5), we obtain

$$(E_z)_{\text{beam loading}} = -\frac{4\lambda_{b0}}{Cl_b^2} z. \tag{6.6}$$

As an example of an intense ion beam pulse of interest for HEDP studies, we take $\lambda_{b0} = 1\ \mu\text{C/m}$ and $l_b = 0.2$ m. With $C = 1/3$ pf/m, a typical value for an oil dielectric helix, the beam loading deceleration with the ion beam remaining in synchronism with the circuit wave is 300 keV/m times the helix length z in meters. The deceleration from beam loading in this simplified limiting case is therefore of order 10% or less of the (desired) 3–4 MeV/m acceleration gradient.

To illustrate the development of this asymptotic solution, "snapshots" at two different times of the voltage induced on a helix by a Gaussian shaped ion beam pulse moving at a constant velocity $v_b = 0.98v_c$ are presented in Fig. 24. The boundary condition on the helix voltage is $V = 0$ at $z = 0$. Note that the main body of the pulse is decelerated at a constant rate, but the "wings" of the ion pulse are actually accelerated for the times and distances illustrated.

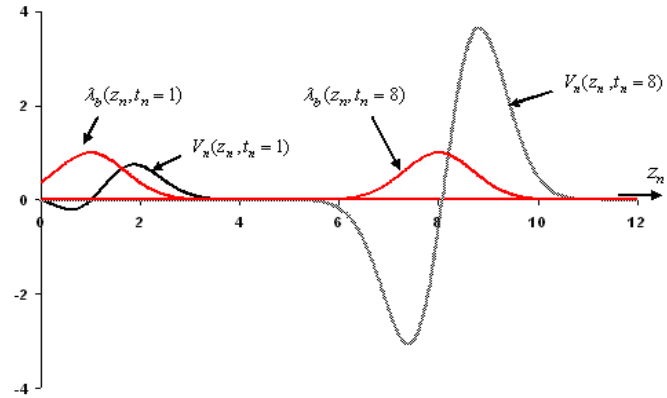

FIG. 24. (Color) Snapshots of the beam loading voltage V induced on the helix by a Gaussian shaped ion beam pulse moving at a constant velocity $v_b = 0.98v_c$. The voltage is normalized as $V_n \triangleq CV(z,t)/\lambda_{b0}$, and the normalized distance and time is $z_n \triangleq 2z/l_b$ and $t_n \triangleq 2v_b\, t/l_b$, respectively. The ion beam line charge density is $\lambda_b = \lambda_{b0}\ \exp\ -(z_n - t_n)^2$.

B. Generalization of the beam loading model to short wavelengths

The formalism developed in Sec. V can be easily generalized to include the contribution of the ion beam to the quasielectrostatic potential ϕ. We use superposition and write the overall potential as $\phi = \phi_c + \phi_b$, where ϕ_b is the contribution of the ion beam and ϕ_c is the "circuit field" described in Sec. V that satisfies the homogeneous Laplace equation inside the helix and is related to the helix voltage by Eq. (5.5). For ϕ_b, in general we must solve

$$\nabla^2\phi_b = -\rho_b(r,z,t)/\varepsilon_0 \tag{6.7}$$

inside the helix subject to the boundary condition $\phi_b(r = a) = 0$, where $\rho_b(r,z,t)$ is the ion beam volume charge density.

With an ion beam line charge density $\lambda_b \sim \exp(-jkz)$, and assuming a relatively "thin" ion beam ($ka_b < 1$), the induced line charge density on the inside of the helix by the ion beam can be shown to be

$$(\lambda_c)_{\text{beam}} = -\lambda_b f_\lambda(k), \tag{6.8}$$

where the "induced charge reduction factor" is defined as

$$f_\lambda(k) \equiv ka\left[K_1(ka) + \frac{I_1(ka)K_0(ka)}{I_0(ka)}\right]. \tag{6.9}$$

At long wavelengths ($ka < 1$), an expansion of Eq. (6.9) shows that $f_\lambda(k) \to 1$ as it should. At short wavelengths, the induced charge on the helix is reduced, eventually falling to zero as $\exp(-ka)$ for $ka \gg 1$.

A second reduction factor in the ion beam dynamics that comes into play at short wavelengths is the ratio of the circuit axial electric field at the beam to the axial field at the helix. With a thin ion beam, the circuit axial electric field that acts on the ions is

$$E_{zc}(r \approx 0) = -f_V(k)\frac{\partial V}{\partial z}, \tag{6.10}$$

where $f_V \equiv 1/I_0(ka)$, the function plotted in Fig. 23.

C. Longitudinal bunching instability ("TWT amplification")

In a traveling wave tube electron beam density and velocity modulations are amplified by their interaction with the traveling wave on the helix. The same mechanism could in principle lead to growth of small perturbations in the ion beam density in the PLIA concept. Since the ion velocity in the PLIA does not remain in close synchronism with the circuit wave, however, we do not expect this mechanism to be a serious limitation. In this section, we present without derivation the dispersion equation for an infinitely long beam pulse in a constant velocity helix, and estimate the gain in "worst case" scenarios.

We consider a thin ion beam with a constant (unperturbed) beam velocity and line charge density, and a constant helix velocity. Small perturbations in the ion beam density and velocity of the form $\exp(j\omega t - jkz)$ create fields on the helix through the image charge source term [Eq. (6.8)] in the generalized version of Eq. (6.1). These fields act back on the ion beam through the axial electric field of the circuit given by Eq. (6.10). For the axial space charge fields of the ion beam itself we use the g-factor description

$$E_{zb} = -\frac{g}{4\pi\varepsilon_0}\frac{\partial \lambda_b}{\partial z}, \tag{6.11}$$

with $g = 1 + 2\ln(a/a_b)$ for a thin beam. With these axial forces and a "cold fluid" model of the ion beam, the following dispersion equation can be derived:

$$1 = Q_b\frac{k^2 v_b^2}{(\omega - kv_b)^2}\left[1 + \alpha_c\frac{\omega^2}{(\omega^2 - k^2 v_c^2)}\right]. \tag{6.12}$$

Here

$$Q_b \equiv \frac{gq\lambda_b}{4\pi\varepsilon_0 M v_b^2} \tag{6.13}$$

is g times the dimensionless perveance, and

$$\alpha_c(k) \equiv f_\lambda(k) f_V(k)\left(\frac{4\pi\varepsilon_0}{g\ C(k)}\right), \tag{6.14}$$

with $C(k)$ the generalized helix capacitance per meter defined in Eq. (5.15).

As a typical example, we consider the oil helix discussed in Sec. II with a helix radius of 8 cm, an outer tube radius of 12 cm, and a beam radius of order 2 cm ($g \sim 3.8$). With $ka < 1$ (for the strongest interaction), $\alpha_c \sim 0.1$. With an ion beam line charge density $\lambda_b \sim 1/3\ \mu$C/m, $Q_b \sim 5 \times 10^{-3}/W_b$, where W_b is the ion beam energy in MeV. We can therefore consider Q_b and α_c as small parameters in developing approximate solutions of the dispersion equation (6.12).

With very small Q_b, the approximate solutions to the dispersion equation are the fast and slow space charge waves $\omega = kv_b \pm \delta$, and the forward and backward traveling circuit waves $\omega = \pm kv_c$. Instability is predicted only over a very narrow ion beam velocity range when the ions are close to synchronism with the forward circuit wave, given roughly by

$$1 < \frac{v_c}{v_b} < (1 + \alpha_c)^{1/2}. \tag{6.15}$$

The maximum gain at synchronism is also very modest. The dispersion equation in that regime can be approximated as a cubic (see Ref. [3]). When $Q_b^{1/2} < \alpha_c/2$, the steady state spatial growth rate is given by

$$\mathrm{Im}\,(k) = k\frac{\sqrt{3}}{2}\left(\frac{Q_b\alpha_c}{2}\right)^{1/3}. \tag{6.16}$$

With $Q_b \sim 10^{-3}$, $\alpha_c \sim 10^{-1}$, and $k \sim 1/a \sim 12\ \mathrm{m}^{-1}$, the maximum gain *at synchronism* is only about one e-fold in 2.5 m. (The finite beam pulse length will also limit the growth, since the unstable wave propagates at a slightly different speed than the ion beam.) We therefore conclude from these rough estimates that the TWT instability is unlikely to be an important factor in the parameter regime we are considering.

VII. CONCLUSIONS

The major attraction of the PLIA concept is the potential for very low development and capital cost, however, realizing this potential will require a relatively high acceleration gradient. Several factors will limit the acceleration gradient:

1. The vacuum insulator must hold the pulsed axial electric field without breakdown. We note that the helix automatically provides "inductive grading" of this stress and the typical time scales are a hundred nanoseconds or less. We believe axial gradients on the vacuum insulator of 3 to 5 MV/m are reasonably conservative goals with a proper design, and more sophisticated insulator designs might substantially increase this vacuum gradient limit.

2. The peak voltage will be limited by breakdown in the dielectric media $[V_0 < a\ln(b/a)E_{r\max}]$; 10–20 MV/m limits on $E_{r\max}$ should be reasonably conservative for oil or epoxy media with pulse lengths of a microsecond or less.

3. The ramp length is limited by the requirement for the major fraction of the axial wave number spectra to be confined to the $ka < 1$ region as discussed in Sec. V. As a rough criterion, we will take this limit to be $l_c > \pi a$.

The combination of limits 2 and 3 gives another limit on the axial accelerating gradient, namely $E_{z\max} \sim E_{r\max}[2\ln(b/a)/\pi]$. With typical design choices of

$b/a \sim 1.5$ and $E_{r\,\max} \sim 10$–20 MV/m, this acceleration gradient limit is also around 3–5 MV/m.

From the beam dynamics standpoint, axial electric fields that can continuously accelerate and focus a slowly moving ion bunch in a PLIA accelerator are attractive features compared to induction architectures with widely separated gaps. The simplicity and experimental flexibility of untapered helical lines, with a broad range of operating modes and energy gains of several MeV/meter with pulse power voltages in the 200–300 keV range, are also attractive. However, many practical problems like control of ion losses, stray electrons, etc. will undoubtedly need to be faced and resolved to realize its potential.

ACKNOWLEDGMENTS

The PLIA concept resulted from a series of brainstorming sessions at LBNL aimed at finding attractive accelerator options for the HEDP application of heavy ion beams. I would like to acknowledge the leadership of Grant Logan and Simon Yu and the sponsorship of the IFE Virtual National Lab at LBNL in stimulating the work reported in this paper. I would also like to acknowledge active collaborations with many other colleagues at LBNL and LLNL in this work, including Will Waldron, Lou Reginato, Alex Friedman, Dave Grote, Enrique Henestroza, Prabir Roy, Joshua Coleman, Frank Bieniosek, John Barnard, Matthaeus Leitner, George Caporaso, and Scott Nelson. This work was sponsored in part by Lawrence Berkeley National Laboratory under the auspices of the U.S. Department of Energy by the University of California, Lawrence Berkeley National Laboratory, Contract No. DE-AC03-76SF00098.

[1] L. Grisham, Phys. Plasmas **11**, 5727 (2004); A. Friedman *et al.*, in *Proceedings of the 2005 Particle Accelerator Conference, Knoxville, Tennessee, 2005* (IEEE Catalog No. 05CH37623C), p. 339; J. J. Barnard *et al.*, *ibid.*, p. 2568.

[2] R. J. Briggs, L. Reginato, and W. Waldron, in *Proceedings of the 2005 Particle Accelerator Conference, Knoxville, Tennessee, 2005* (Ref. [1]), p. 440; W. Waldron, L. Reginato, and R. J. Briggs, *ibid.*, p. 2092.

[3] W. H. Louisell, *Coupled Mode and Parametric Electronics* (John Wiley and Sons, Inc., New York, 1960).

[4] E. Henestroza, C. Peters, S. Yu, D. Grote, and R. J. Briggs, in *Proceedings of the 2005 Particle Accelerator Conference, Knoxville, Tennessee, 2005* (Ref. [1]), p. 2032.

[5] G. J. Caporaso, R. J. Briggs, B. Poole, and S. D. Nelson, in *Proceedings of the 2005 Particle Accelerator Conference, Knoxville, Tennessee, 2005* (Ref. [1]), p. 2330.

[6] S. D. Nelson, R. J. Briggs, G. J. Caporaso, A. Friedman, B. Poole, and W. Waldron, in *Proceedings of the 2005 Particle Accelerator Conference, Knoxville, Tennessee, 2005* (Ref. [1]), p. 2485.

[7] R. M. Fano, L. J. Chu, and R. B. Adler, *Electromagnetic Fields, Energy, and Forces* (John Wiley and Sons, Inc., New York, 1960), pp. 256–259.

[8] Alex Friedman, Lawrence Livermore National Laboratory Report No. UCRL-TR-218776, 2006; available upon request from the LLNL Library, or from the author via email at af@llnl.gov.